mater.scichina.com link.springer.com

Published online 28 April 2022 | https://doi.org/10.1007/s40843-022-2001-7
Sci China Mater 2022, 65(10): 2675–2684

Temperature-controlled synthesis of heterostructured Ru-Ru_2P nanoparticles embedded in carbon nanofibers for highly efficient hydrogen production

Yue Wei[1], Gao Xu[2], Yujie Wei[1], Lvlv Ji[1*], Tao Wang[1], Zhun Liu[2*] and Sheng Wang[1*]

ABSTRACT **Developing highly efficient, cost-effective, and stable electrocatalysts for hydrogen evolution reaction (HER) is of considerable importance but remains challenging. Herein, we report the fabrication of a robust Ru-based electrocatalyst, which comprises heterostructured Ru-Ru_2P nanoparticles that are embedded in the N,P-codoped carbon nanofibers (CNFs), through a synthetic strategy involving electrospinning and temperature-controlled pyrolysis treatment. The as-prepared Ru-Ru_2P catalyst (Ru-Ru_2P@CNFs) shows excellent HER catalytic activities with low overpotentials of 11 and 14 mV in acidic and alkaline media, respectively, to achieve a current density of 10 mA cm^{-2}, which are superior to the individual components of pure Ru and Ru_2P catalysts. Density functional theory calculations demonstrate the existence of electronic coupling effect between Ru and Ru_2P at the heterointerfaces, leading to a well-modulated electronic structure with optimized hydrogen adsorption strength and enhanced electrical conductivity for efficient HER electrocatalysis. In addition, the overall synthetic strategy can be generalized for the synthesis of a series of transitional metal phosphide-based nanofibers, thereby holding a remarkable capacity for various potential applications.**

Keywords: hydrogen evolution reaction, Ru-based electrocatalysts, heterostructure, carbon nanofibers, electrocatalysis

INTRODUCTION

Hydrogen, which has high energy density and excellent conversion properties, is considered an ideal energy carrier to replace traditional fossil fuels [1]. Hydrogen production *via* electrocatalytic water splitting is recognized as a promising and sustainable process, preferably when the applied electricity is derived from renewable energy sources (such as solar and wind energy) [2]. Highly active electrocatalysts are indispensable for cathodic hydrogen evolution reaction (HER) and anodic oxygen evolution reaction to achieve efficient water splitting [3–5]. Platinum (Pt)-based materials are regarded as the benchmark electrocatalysts for HER, but their large-scale applications are limited by the high cost and earth rarity of Pt [6]. In the past decade, extensive efforts have been devoted to developing various low-cost HER electrocatalysts, such as noble metal-free or metal-free electrocatalysts, but their catalytic activities remain unsatisfied [7].

Ruthenium (Ru), which has Pt-like hydrogen bonding strength (~65 kcal mol^{-1}) and relatively low price (only ~4% of Pt), has received increasing attention for HER [8]. Various Ru-based materials, including metallic Ru, single atomic Ru, Ru-based alloys, Ru phosphides, and Ru chalcogenides, have been designed and synthesized for HER electrocatalysis, thereby demonstrating excellent catalytic performances [9]. For example, Zheng *et al.* [10] reported that metallic Ru exhibited a pronounced effect of the crystal structure on the HER catalytic activity, and the anomalously structured Ru catalyst showed 2.5 times higher HER turnover frequency than that of Pt in alkaline media. Liu *et al.* [11] synthesized ultrasmall Ru_2P nanoparticles loaded on reduced graphene oxide nanosheets, which possessed a lower HER overpotential than commercial 20 wt% Pt/C.

The catalytic activities of HER electrocatalysts are dominantly dependent on the intrinsic catalytic activity of the active sites, which are generally evaluated by the free energy of hydrogen adsorption (ΔG_{H^*}). A small $|\Delta G_{H^*}|$ value represents a high catalytic activity [12]. Various strategies have been applied to modulate the electronic structures of active sites to boost the intrinsic catalytic activities of Ru-based materials. The strategies include nonmetal doping, transition metal doping, and support engineering [8]. Interface engineering has gradually been recognized as an effective strategy to improve the intrinsic catalytic activity of hybrid nanomaterials due to the electronic coupling and/or interfacial synergistic effect [13]. The interface charge redistribution will be triggered by the combination of different active components, which provide opportunities to optimize the electronic structure for boosted catalytic performance [14]. This strategy is effective for a diversity of transition metal-based electrocatalysts categories [15–21]. Thus, further promoting the intrinsic catalytic activities of Ru-based electrocatalysts by interface engineering strategy is expected, while related investigations are rarely reported for Ru-based electrocatalysts.

Electrocatalysts with well-defined nanostructures are highly desirable to increase the number of accessible catalytic active sites [22]. Among various nanostructures, one-dimensional (1D) nanostructured (such as nanofibers and nanowires) electrocatalysts are advantageous in providing abundant active sites in the radial direction and facilitating rapid electron transfer along the axial direction [23,24]. Electrospinning is a simple and

[1] School of Materials Science and Engineering, Zhejiang Sci-Tech University, Hangzhou 310018, China
[2] Department of Physics, Shaoxing University, Shaoxing 312000, China
* Corresponding authors (emails: llji@zstu.edu.cn (Ji L); liu6zhun@163.com (Liu Z); wangsheng571@hotmail.com (Wang S))

scalable method for the fabrication of 1D nanofibers with controllable compositions for various applications [25]. For HER electrocatalysis, the electrospun carbon nanofibers (CNFs) are applied for loading catalytic active species, which is recognized as an effective strategy to achieve increased catalytic active sites and enhanced conductivity [26].

Herein, we report the design and synthesis of heterostructured Ru-Ru_2P nanoparticles that are *in situ* embedded in N,P-codoped CNFs (denoted as Ru-Ru_2P@CNFs). Nanofibers of polyacrylonitrile (PAN) doped with phytic acid (PA) and $RuCl_3$ (denoted as Ru-PA@PAN) were first prepared by electrospinning, followed by pyrolysis treatment at high temperatures to obtain Ru-Ru_2P@CNFs. Notably, the pyrolysis temperature can significantly dominate the composition and morphology of the resultant nanofibers. The resultant product experiences a composition conversion from pure Ru_2P (750°C) to heterostructured Ru-Ru_2P (800°C) and pure Ru (850°C) with an increase in pyrolysis temperature. Among these products, Ru-Ru_2P@CNFs possess the highest HER catalytic activities with ultralow overpotentials of 11 and 14 mV at 10 mA cm^{-2} in acidic and alkaline media, respectively, which is even superior to the commercial 20% Pt/C and the recently reported Ru-based electrocatalysts. Strong electronic redistribution occurs at the heterointerface of Ru-Ru_2P, which modulates the electronic structure to achieve an optimized hydrogen adsorption strength, based on the density functional theory (DFT) calculations. In addition, the morphology of 1D nanofibers is beneficial to exposing additional accessible active sites and facilitating mass transfer for enhanced HER electrocatalysis. The overall synthetic strategy can be extended to prepare a series of transitional metal phosphide (TMP)-based nanofibers, indicating the versatility of this synthetic strategy.

EXPERIMENTAL SECTION

Reagents

Ruthenium(III) chloride trihydrate (98%, $RuCl_3{\cdot}3H_2O$), bis(acetylacetonate)dioxomolybdenum(VI) (97%, $C_{10}H_{14}MoO_6$), tungsten(VI) chloride (99.9%, WCl_6), and PA solution (70%, $C_6H_{18}O_{24}P_6$) were purchased from Macklin Reagents Ltd. Nickel acetate tetrahydrate (99.9%, $NiC_4H_6O_4{\cdot}4H_2O$) and copper acetate monohydrate (99.95%, $C_4H_6CuO_4{\cdot}H_2O$) were purchased from Aladdin Reagents Ltd. PAN (M_w = 150,000), 20% Pt/C, and *N*,*N*-dimethylformamide (>99.5%, DMF) were purchased from Sigma-Aldrich Co. High-purity air and argon (99.999%) gases were purchased from Hangzhou Gases Co. All other chemical reagents were of analytical grade and used as received without further purification. All electrolyte solutions were prepared with Milli-Q ultrapure water (18 MΩ cm).

Characterizations

Fourier transform infrared (FT-IR) spectra were obtained on a Nicolet 6700 spectrometer (Thermo Fisher Nicolet, USA) with KBr pellets. X-ray diffraction (XRD) patterns were measured by a Rigaku D/max-2200 *via* ceramic monochromatized Cu-Kα radiation (λ = 0.154 nm) operated at 40 kV and 40 mA. The scanning rate was set as 2° min^{-1}, and the scanning range was set as 20°–80°. Raman spectra were recorded on a confocal microscope laser Raman spectrometer (Renishaw inVia).

Scanning electron microscopy (SEM) images and energy-dispersive X-ray spectrometer (EDX) spectra were recorded at ZEISS VLTRA-55 equipped with a Horiba EDX system. SEM images and EDX spectra were respectively recorded with an acceleration voltage of 3 and 10 kV. Transmission electron microscopy (TEM) and high-resolution TEM (HRTEM) images were recorded on JEM-2010 HR.

X-ray photoelectron spectroscopy (XPS) for elemental analysis was conducted on a Kratos Axis Ultra DLD X-ray Photoelectron Spectrometer using 100 W monochromated Al Kα radiation as the X-ray source for excitation. The 500-μm X-ray spot was used for XPS analysis. The base pressure in the analysis chamber was approximately 3×10^{-10} mbar (1 bar = 100 kPa). The C 1s peak (284.6 eV) was used for internal calibration. The peak resolution and fitting were processed with the XPS Peak 41 software.

The Brunauer-Emmett-Teller (BET) surface areas were measured on a Quanta Chrome Nova 2200e by N_2 adsorption at 77.4 K. The samples were degassed for 3 h at 300°C before measurements.

The inductively coupled plasma-optical emission spectrometry (ICP-OES) measurements were conducted on a Perkin Elmer ICP-OES Optima 8300. The sample was dissolved in concentrated HNO_3 by oil-bath heating at 80°C for 24 h. The weight percentage of the Ru element was calculated and analyzed by using the working curve method.

Synthesis of Ru-PA@PAN and PAN nanofibers

The hybrid Ru-PA@PAN nanofibers were synthesized by the electrospinning method. Briefly, $RuCl_3{\cdot}3H_2O$ (1 mmol), PA (0.5 g), and PAN (1 g) were dissolved in 9 mL of DMF by continuous stirring overnight at room temperature to obtain the homogeneous mixed solution. Afterward, the mixed solution was loaded into a plastic syringe equipped with a stainless steel needle. A revolving Al foil was applied for the collection of electrospun nanofibers, and the distance between the needle tip and Al foil was maintained at 20 cm. A high voltage of 13 kV was applied between the needle and Al foil to trigger the electrospinning, and the solution feeding speed was set as 0.25 mL h^{-1}. The temperature and humidity were respectively controlled at around 30°C and 44% during the electrospinning. The obtained Ru-PA@PAN nanofibers were dried in a vacuum oven at 60°C for 12 h after electrospinning for 10 h.

In a control experiment, pure PAN nanofibers were synthesized under identical conditions without $RuCl_3{\cdot}3H_2O$ and PA.

Synthesis of Ru-Ru_2P@CNFs, Ru_2P@CNFs, Ru@CNFs, and CNFs

The hybrid Ru-PA@PAN precursor was first pre-oxidized at 270°C in the air for 1 h with a heating rate of 1°C min^{-1} to synthesize Ru-Ru_2P@CNFs, followed by pyrolysis at 800°C under Ar atmosphere for 2 h with a heating rate of 2°C min^{-1}.

Ru_2P@CNFs and Ru@CNFs were synthesized in the control experiments under identical conditions, except for the pyrolysis temperature at 750 and 850°C, respectively. CNFs were synthesized by the identical synthetic procedure for Ru-Ru_2P@CNFs, except that pure PAN nanofibers were used as precursors instead of Ru-PA@PAN.

Synthesis of $Ni_{12}P_5$-Ni_2P@CNFs, Cu-Cu_3P@CNFs, MoP@CNFs, and WP@CNFs

Briefly, the precursors Ni-PA@PAN, Cu-PA@PAN, Mo-PA@PAN, and W-PA@PAN were first synthesized by the identical electrospinning method for the synthesis of Ru-PA@PAN; instead of $RuCl_3{\cdot}3H_2O$, $NiC_4H_6O_4{\cdot}4H_2O$, C_4H_6-

$CuO_4{\cdot}H_2O$, $C_{10}H_{14}MoO_6$, and WCl_6 were used. Afterward, $Ni_{12}P_5$-Ni_2P@CNFs, Cu-Cu_3P@CNFs, MoP@CNFs, and WP@CNFs were accordingly synthesized by the identical synthetic procedure for Ru-Ru_2P@CNFs with Ru-PA@PAN, Ni-PA@PAN, Cu-PA@PAN, Mo-PA@PAN, and W-PA@PAN as the precursors.

Electrochemical measurements

Electrochemical measurements were conducted on an electrochemical workstation (CHI 660E, Chenhua, China) with a standard three-electrode setup. The setup comprised a working electrode, a carbon rod counter electrode, and a saturated calomel reference electrode. The electrocatalyst (4 mg) and Nafion solution (5 wt%, 80 μL) were first dispersed in 1 mL of 4:1 (*v*/*v*) water/ethanol to prepare the working electrode. Then, the electrocatalyst suspension (5 μL) was dropped onto the surface of the glassy carbon electrode (mass loading: ~0.26 mg cm^{-2}), followed by drying at room temperature.

The HER performances of electrocatalysts were evaluated in N_2-saturated 0.5 mol L^{-1} H_2SO_4 and 1 mol L^{-1} KOH. The reported potentials were referred to the reversible hydrogen electrode (RHE) *via* the Nernst equation: $E_{RHE} = E_{SCE} + 0.059pH + 0.244$, which were experimentally calibrated considering RHE in the high-purity H_2-saturated electrolyte with a Pt sheet as the working electrode. In 0.5 mol L^{-1} H_2SO_4, $E_{RHE} = 0.273\ V + E_{SCE}$; in 1 mol L^{-1} KOH, $E_{RHE} = 1.05\ V + E_{SCE}$. Unless stated otherwise, linear sweep voltammetry (LSV) was conducted at a scan rate of 2 mV s^{-1}. The Tafel slope was obtained from the LSV plot using a linear fit applied to points in the Tafel region. Electrochemical impedance spectroscopy (EIS) measurements were conducted from 10^{-2} to 10^5 Hz with an amplitude of 5 mV at the applied potentials. The electrochemical stability of the electrocatalyst was conducted by cyclic voltammetry (CV) scanning and long-term electrolysis. CV scanning with different scan rates within the potential range of 0–0.2 V *vs.* RHE in 1 mol L^{-1} KOH was also conducted to evaluate the electrochemical double-layer capacitance (C_{dl}) of the electrocatalysts. Unless stated otherwise, LSV and Tafel data plots were corrected with 90% *iR* compensation. The experiments were all performed at 22 ± 2°C.

DFT calculations

DFT calculations were conducted with the Vienna *ab initio* simulation package. The revised Perdew-Bruke-Ernerhof approach within the generalized gradient approximation was employed for the electronic exchange-correlation functional. The kinetic plane-wave cutoff was set as 520 eV, and the convergence threshold of the atoms was set as 10^{-6} eV and 2×10^{-3} eV $Å^{-1}$ in energy and force, respectively. The Brillouin zone was sampled by the Monkhorst-Pack method with a grid spacing of less than $2\pi \times 0.02\ Å^{-1}$. The in-plane heterostructure of Ru-Ru_2P [110] was created by connecting the lattice surfaces of Ru (110) and Ru_2P (110). The surface slab model can be obtained by a vacuum spacing larger than 30 Å to avoid the spurious interactions along the [111] direction. Thus, the (111) surface of the Ru-Ru_2P [110] heterostructure was constructed by a 5 × 2 orthorhombic supercell to compare the adsorption differences with the pure Ru_2P and Ru (111) surfaces. The hydrogen adsorption energies on the (111) surfaces of Ru-Ru_2P [110] heterostructure, Ru_2P, and Ru were calculated considering the gas phase of hydrogen using the following equation:

$$\Delta E_{H^*} = E(H^*) - E(*) - E(H_2)/2, \quad (1)$$

where $E(H^*)$, $E(*)$, and $E(H_2)$ are the calculated energies of the adsorbed hydrogen atom on the surface, a clean surface, and molecule hydrogen in the gas phase, respectively.

The Gibbs free energies of hydrogen adsorption on the surfaces of Ru-Ru_2P [110] heterostructure, Ru_2P, and Ru were calculated using the following:

$$\Delta G_{H^*} = \Delta E_{H^*} + \Delta E_{ZPE} - T\Delta S, \quad (2)$$

where the ΔE_{ZPE} is the change in zero-point energy of surface vibrations upon hydrogen adsorption, T is the temperature and ΔS is the entropy of adsorption, which is approximated by half the entropy of molecular hydrogen in the gas phase. The calculated value of $(\Delta E_{ZPE} - T\Delta S) \approx 0.24$ eV was adopted in this study by reasonable estimation; therefore, $\Delta G_{H^*} = \Delta E_{H^*} + 0.24$ eV [27].

RESULTS AND DISCUSSION

Synthesis and characterization of electrocatalysts

The synthesis procedures of Ru_2P@CNFs, Ru-Ru_2P@CNFs, and Ru@CNFs are shown in Scheme 1. $RuCl_3{\cdot}3H_2O$, PA, and PAN were first dissolved in DMF, and the mixed solution was then electrospun with a high applied voltage of 13 kV to form a hybrid PAN nanofiber membrane. PA crosslinked Ru complexes were homogeneously distributed in PAN nanofibers during the

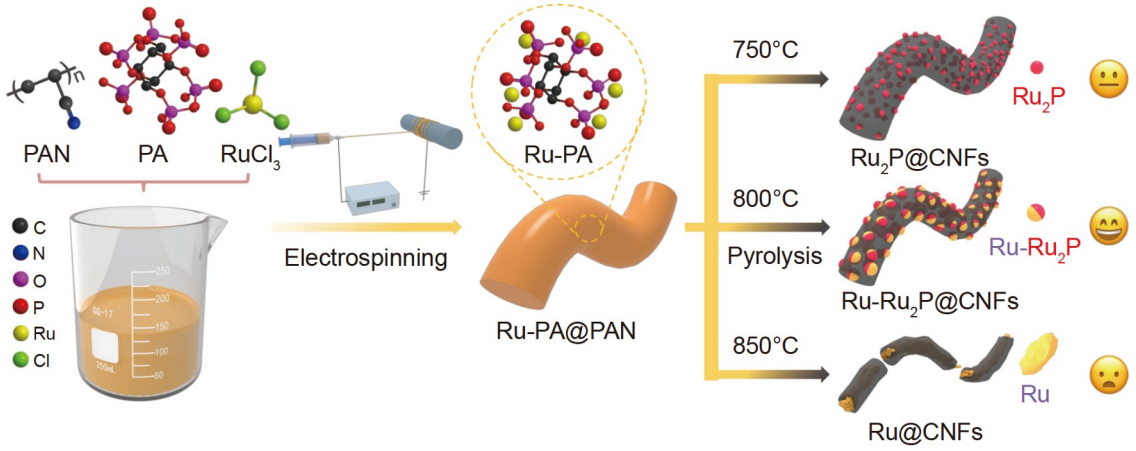

Scheme 1 Temperature-controlled synthesis route of Ru_2P@CNFs, Ru-Ru_2P@CNFs, and Ru@CNFs.

electrospinning process. The as-prepared Ru-PA@PAN hybrid precursor was first preoxidized in the air at 270°C for 1 h and then further pyrolyzed under an Ar atmosphere at a high temperature for 2 h. Ru_2P@CNFs, Ru-Ru_2P@CNFs, and Ru@CNFs were respectively prepared at 750, 800, and 850°C based on the pyrolysis temperature in an Ar atmosphere.

Fig. 1a, b show the SEM images of Ru-PA@PAN, which exhibits continuous nanofiber structures with a diameter of around 500 nm. Fig. 1c shows the FT-IR spectra of PAN, PA, $RuCl_3$, and Ru-PA@PAN. The FT-IR spectrum of Ru-PA@PAN exhibits two characteristic peaks of PAN at 1450 and 2243 cm^{-1}, which can be ascribed to the characteristic peaks of $-CH_2$ and C≡N in PAN [28]. Moreover, the feature peaks of PA at around 1000 and 1640 cm^{-1} are observed in the FT-IR spectrum of Ru-PA@PAN [29], whereas that of $RuCl_3$ is hardly identified, indicating the formation of PA crosslinked Ru complexes in the PAN matrix.

Fig. 1d exhibits the XRD patterns of samples obtained by pyrolyzing the Ru-PA@PAN precursor at 750, 800, and 850°C. These patterns reveal that the pyrolysis temperature could significantly dominate the composition and crystal phase of the electrocatalysts. The product at 750°C comprises a pure crystal phase of Ru_2P (JCPDS no. 65-2382). An additional crystal phase of metallic Ru (JCPDS no. 06-0663) appears along with Ru_2P by elevating the temperature to 800°C. The crystal phase of Ru_2P disappears at a high temperature of 850°C, and only a pure crystal phase of Ru is obtained. The XRD results demonstrate a crystal phase conversion from Ru_2P to Ru by increasing the pyrolysis temperature from 750 to 850°C.

The elemental compositions and electronic states of Ru_2P@CNFs, Ru-Ru_2P@CNFs, and Ru@CNFs were probed by XPS. The XPS survey spectra in Fig. S1 exhibit the coexistence of P, Ru, C, N, and O in these pyrolyzed samples, and Fig. 1e shows their high-resolution Ru 3p XPS spectra. The doublet peaks of Ru $3p_{3/2}$ and Ru $3p_{1/2}$ in Ru_2P@CNFs are respectively located at 462.4 and 484.5 eV, whereas these peaks are increasingly negative shifted in Ru-Ru_2P@CNFs (462 and 484.2 eV) and Ru@CNFs (461.6 and 483.6 eV). The negative shift of Ru 3d peaks with an increase in pyrolysis temperature reveals a decrease in Ru valence state in the resultant pyrolyzed samples. The high-resolution P 2p XPS spectra of these samples are shown in Fig. 1f. The P 2p XPS spectra can be all fitted into two

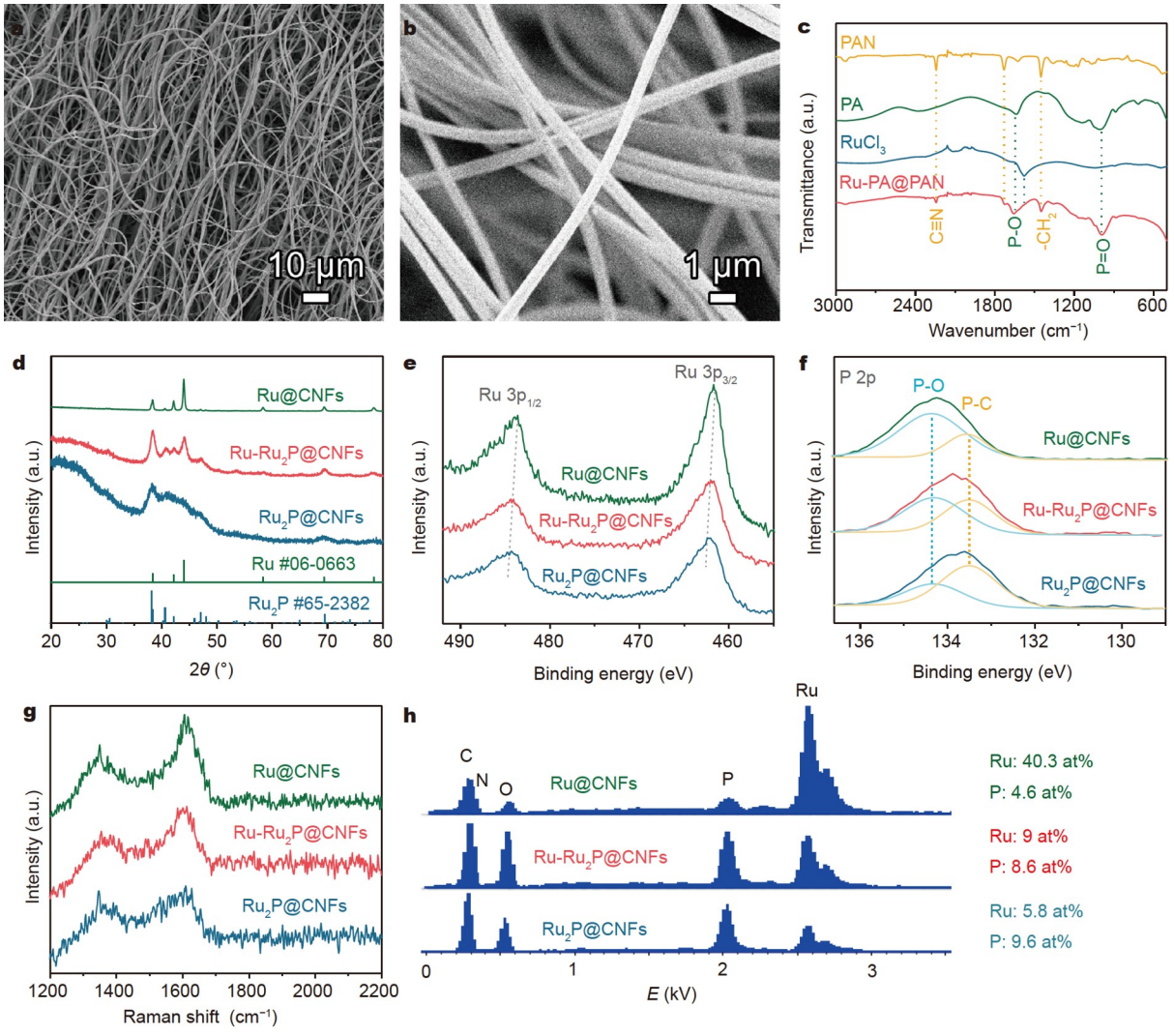

Figure 1 (a, b) SEM images of Ru-PA@PAN. (c) FT-IR spectra of PAN, PA, $RuCl_3$, and Ru-PA@PAN. (d) XRD patterns, (e) high-resolution Ru 3p XPS spectra, (f) high-resolution P 2p XPS spectra, (g) Raman spectra and (h) EDX spectra of Ru_2P@CNFs, Ru-Ru_2P@CNFs, and Ru@CNFs.

peaks located at 133.5 and 134.3 eV, which are indexed to the bonding state of P–C and P–O, respectively [30]. Notably, the peak intensity/area of P–C is decreased with the increase in the pyrolysis temperature, whereas that of P–O is contrarily increasing. The Ru-P feature peaks at the region of 129–131 eV for Ru_2P@CNFs and Ru-Ru_2P@CNFs are not observed [31], which may be ascribed to the dominant existence of P–C and P–O bonding states at the sample surface. The peak fitting of high-resolution C 1s and N 1s XPS spectra in Fig. S2 suggests that the carbon matrix arising from the pyrolysis of PAN has been codoped with N and P atoms. The N,P-codoped carbon matrix can endow the catalyst with high conductivity and hydrophilicity, which respectively favor the electron transfer and electrolyte contact [30].

Fig. 1g shows the Raman spectra of Ru_2P@CNFs, Ru-Ru_2P@CNFs, and Ru@CNFs. Two distinct peaks at around 1355 and 1610 cm^{-1} are respectively attributed to the D- and G-bands of the carbon-based materials [32]. The D- and G-bands for the Raman spectra are respectively related to the disordered graphitic and graphite carbons. The I_D/I_G peak intensity ratios for Ru_2P@CNFs, Ru-Ru_2P@CNFs, and Ru@CNFs are 0.83, 0.68, and 0.57, respectively, indicating that a high degree of graphitization can be obtained at a high pyrolysis temperature. Fig. 1h shows that the EDX spectra of these samples reveal a decrease in P content and an increase in Ru content by raising the pyrolysis temperature, which is consistent with the XRD results. Moreover, the weight percentage of the Ru element in these samples was determined by ICP-OES. The analysis of the working curve reveals 25.8, 36.4, and 75.6 wt% of Ru element in Ru_2P@CNFs, Ru-Ru_2P@CNFs, and Ru@CNFs, respectively. The interesting phase conversion from Ru_2P to Ru may be attributed to the carbothermal reduction based on the aforementioned characterizations. In carbothermal reduction, the carbon source acts as the reducing agent to decrease Ru_2P into metallic Ru at a high pyrolysis temperature (for instance, 850°C).

The morphologies of Ru_2P@CNFs, Ru-Ru_2P@CNFs, and Ru@CNFs were characterized by SEM and TEM. Fig. 2a, b respectively reveal the SEM images of Ru_2P@CNFs and Ru-Ru_2P@CNFs, which demonstrate that the morphologies of nanofibers are well retained after the pyrolysis. However, the nanofibers in the SEM image of Ru@CNFs obtained at 850°C (Fig. 2c) are fractured and aggregated. Fig. 2d–f show the TEM images of a single nanofiber for these pyrolyzed samples. The diameter of resultant nanofibers is decreased from around 210 to 120 nm with an increase in pyrolysis temperature from 750 to 850°C. Numerous small nanoparticles with a diameter of around

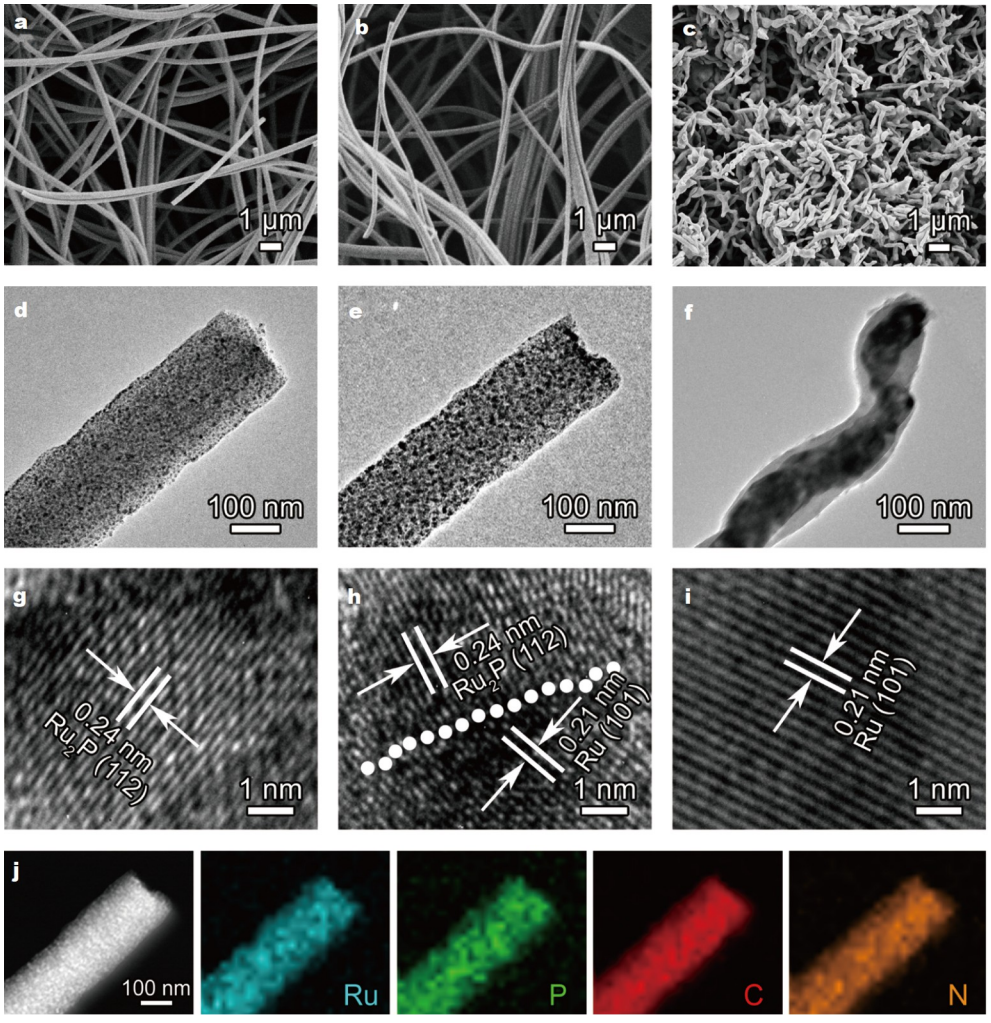

Figure 2 (a–c) SEM images, (d–f) TEM images, and (g–i) HRTEM images of the pyrolyzed samples: (a, d, g) Ru_2P@CNFs, (b, e, h) Ru-Ru_2P@CNFs, and (c, f, i) Ru@CNFs. (j) TEM-EDX elemental mapping images of Ru, P, C, and N on Ru-Ru_2P@CNF.

5 nm in the TEM image of Ru_2P@CNFs (Fig. 2d) are uniformly distributed in the carbon matrix (Fig. S3a). Fig. 2e and Fig. S3b show that the diameter of nanoparticles is increased to around 12 nm for Ru-Ru_2P@CNFs and is further grown and aggregated to large-sized particles for Ru@CNFs (Fig. 2f). The HRTEM image of Ru_2P@CNFs in Fig. 2g exhibits lattice fringes with a *d*-spacing of 0.24 nm, consistent with the (112) crystal plane of Ru_2P [11]. Fig. 2h reveals that the HRTEM image of Ru-Ru_2P@CNFs demonstrates the heterointerface between the (101) plane of Ru and the (112) plane of Ru_2P, which is in accordance with the lattice fringe spacing of 0.21 and 0.24 nm, respectively. Moreover, the HRTEM image of Ru@CNFs identifies the (101) plane of Ru (Fig. 2i). The HRTEM results are consistent with the XRD, XPS, and EDX characterizations, confirming the successful fabrication of Ru_2P@CNFs, Ru-Ru_2P@CNFs, and Ru@CNFs. Fig. 2j shows that the TEM-EDX elemental mapping images of Ru-Ru_2P@CNFs illustrate the uniform distribution of Ru, P, C, and N elements throughout the nanofiber. This finding further demonstrates that numerous heterostructured Ru-Ru_2P nanoparticles are uniformly embedded on the N,P-codoped carbon matrix. Fig. S4 shows that the BET surface area of Ru-Ru_2P@CNFs is 39.8 $m^2 g^{-1}$, which is higher than those of Ru_2P@CNFs (21.3 $m^2 g^{-1}$) and Ru@CNFs (26.3 $m^2 g^{-1}$).

Electrocatalytic HER performance

A typical three-electrode setup was applied to evaluate the HER catalytic performances of Ru_2P@CNFs, Ru-Ru_2P@CNFs, and Ru@CNFs in 0.5 mol L^{-1} H_2SO_4. For comparison, commercial 20% Pt/C and Ru-free CNFs were also examined under identical experimental conditions. The LSV curves of the electrocatalysts are shown in Fig. 3a. CNFs show a negligible catalytic activity, but their catalytic performance is significantly enhanced by loading with catalytic active nanoparticles. Ru-Ru_2P@CNFs exhibit higher catalytic activity than Ru_2P@CNFs, Ru@CNFs, and even 20% Pt/C. The required overpotentials are 11, 12, 25, and 152 mV for Ru-Ru_2P@CNFs, 20% Pt/C, Ru_2P@CNFs, and Ru@CNFs, respectively, to achieve an HER catalytic current density of 10 mA cm^{-2}. In line with the LSV results, Ru-Ru_2P@CNFs show a smaller Tafel slope of 24.5 mV dec^{-1} than 20% Pt/C (33.5 mV dec^{-1}), Ru_2P@CNFs (44.5 mV dec^{-1}), and Ru@CNFs (94.5 mV dec^{-1}), revealing the most favorable HER catalytic kinetics for Ru-Ru_2P@CNFs (Fig. 3b). In addition, the HER catalytic performance of Ru-Ru_2P@CNFs is even superior to the recently reported Ru-based electrocatalysts in acidic media (Fig. 3c and Table S1).

EIS measurements were conducted to provide further insight into the catalytic kinetics [33]. Nyquist plots of Ru_2P@CNFs, Ru-Ru_2P@CNFs, and Ru@CNFs under an overpotential of 50 mV are shown in Fig. 3d. The figure reveals that the electrode of Ru-Ru_2P@CNFs possesses the smallest charge-transfer resistance (R_{ct}) of around 36 Ω compared with that of Ru_2P@CNFs (62 Ω) and Ru@CNFs (153 Ω), which is consistent with the superior catalytic activity of the former.

Continuous CV scans were conducted from −0.1 to 0.1 V *versus* RHE at a scan rate of 100 mV s^{-1} in 0.5 mol L^{-1} H_2SO_4 to evaluate the catalytic durability of Ru-Ru_2P@CNFs. Fig. 3e shows that the LSV curve of Ru-Ru_2P@CNFs is well-preserved with negligible degradation after 3000 cycles. Moreover, the catalytic durability of Ru-Ru_2P@CNFs was further evaluated by long-term electrolysis at an overpotential of 10 mV (Fig. 3e inset). The HER catalytic current density is sustainable for more than 10 h, confirming the high catalytic durability of Ru-

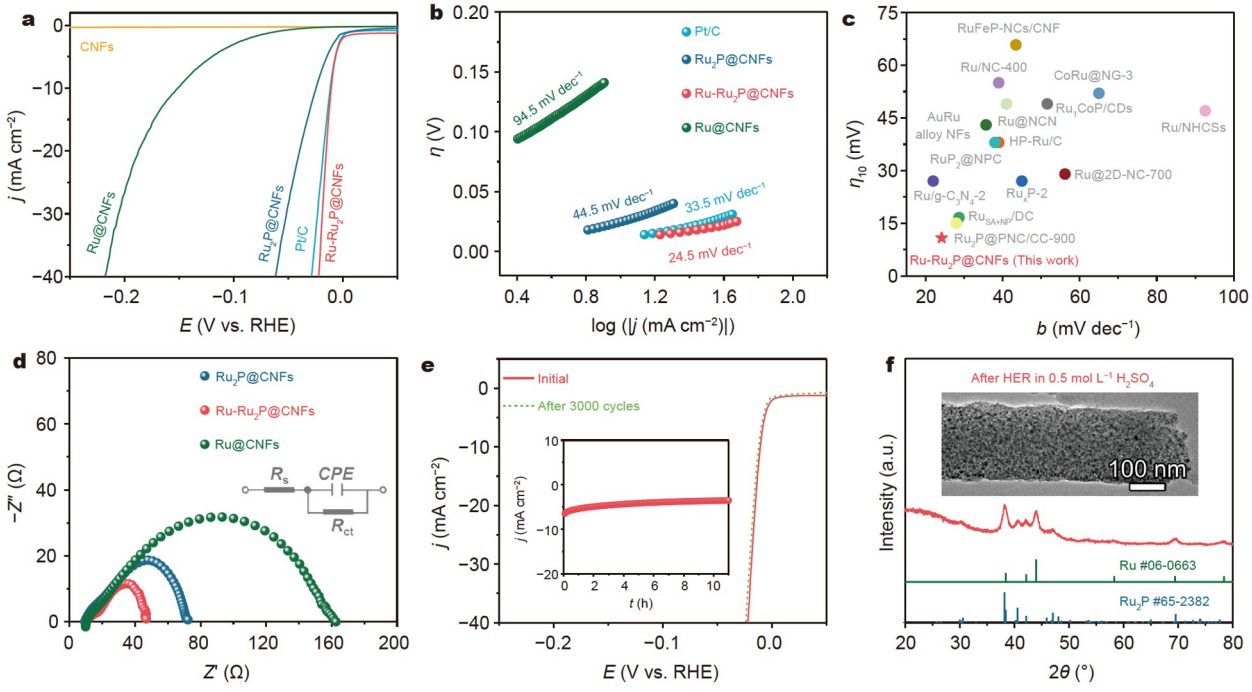

Figure 3 (a) LSV curves and (b) Tafel plots of the electrocatalysts for HER in 0.5 mol L^{-1} H_2SO_4. (c) Comparison of overpotential at 10 mA cm^{-2} (η_{10}) and Tafel slope (*b*) for Ru-Ru_2P@CNFs with the recently reported Ru-based electrocatalysts in 0.5 mol L^{-1} H_2SO_4. (d) Nyquist plots of Ru_2P@CNFs, Ru-Ru_2P@CNFs, and Ru@CNFs at an overpotential of 50 mV in 0.5 mol L^{-1} H_2SO_4 (inset: equivalent electrical circuit used to model the EIS data). (e) LSV curves of Ru-Ru_2P@CNFs before and after 3000 CV cycles in 0.5 mol L^{-1} H_2SO_4. Inset: Long-term electrolysis of Ru-Ru_2P@CNFs at an overpotential of 10 mV in 0.5 mol L^{-1} H_2SO_4. (f) XRD pattern and TEM image (inset) of Ru-Ru_2P@CNFs after long-term electrolysis in 0.5 mol L^{-1} H_2SO_4.

Ru_2P@CNFs in acidic media. The structure and morphology of Ru-Ru_2P@CNFs were respectively characterized by XRD and TEM after the long-term electrolysis. The XRD pattern and TEM image in Fig. 3f respectively show the unchanged crystal phases and the well retained nanofiber morphology, demonstrating the excellent catalytic stability of Ru-Ru_2P@CNFs.

The HER catalytic performances of the samples were also evaluated in 1 mol L^{-1} KOH. Ru-Ru_2P@CNFs in Fig. 4a, b show a higher HER catalytic performance than 20% Pt/C, Ru_2P@CNFs, and Ru@CNFs, featuring a small overpotential of 14 mV to achieve a current density of 10 mA cm^{-2} and a small Tafel slope of 24.2 mV dec^{-1} in 1 mol L^{-1} KOH. The values found herein are also superior to the recently reported Ru-based electrocatalysts in alkaline media (Fig. 4c and Table S2). In addition, a summary of the HER catalytic performances of Ru_2P@CNFs, Ru-Ru_2P@CNFs, and Ru@CNFs is listed in Table S3. Nyquist plots in Fig. S5 show that Ru-Ru_2P@CNFs possess a decreased value for R_{ct} than Ru_2P@CNFs and Ru@CNFs, demonstrating a high HER catalytic activity for Ru-Ru_2P@CNFs in alkaline media. The HER catalytic durability of Ru-Ru_2P@CNFs was examined by continuous CV scans and long-term electrolysis in 1 mol L^{-1} KOH. Electrocatalysis degradation is hardly observed for Ru-Ru_2P@CNFs after 3000 CV cycles or 11 h electrolysis (Fig. 4d), and the XRD pattern of Ru-Ru_2P@CNFs is unchanged after the electrolysis (Fig. S6), demonstrating the excellent catalytic stability of Ru-Ru_2P@CNFs in alkaline media.

The electrochemical double-layer capacitance (C_{dl}) at the solid-liquid interface was measured by CVs with different scan rates within the potential range of 0–0.2 V *versus* RHE in 1 mol L^{-1} KOH (Fig. S7) to assess the electrochemically active surface area (ECSA) of the catalysts. Fig. 4e shows that the C_{dl} value of Ru-Ru_2P@CNFs is calculated as 64.1 mF cm^{-2}, which is larger than those of Ru_2P@CNFs (23.5 mF cm^{-2}) and Ru@CNFs (10.1 mF cm^{-2}), indicating a large ECSA and additional abundant catalytic active sites for Ru-Ru_2P@CNFs. LSV curves of Ru_2P@CNFs, Ru-Ru_2P@CNFs, and Ru@CNFs were normalized by the ECSA to compare the specific activity. Fig. 4f shows the ECSA-normalized LSV curves, revealing the higher intrinsic catalytic activity for Ru-Ru_2P@CNFs than Ru_2P@CNFs and Ru@CNFs.

DFT calculations

The DFT calculations were conducted to provide deep insights into the excellent HER catalytic activity of Ru-Ru_2P@CNFs. A reasonable model of Ru-Ru_2P [110] heterostructure was constructed with a small interfacial strain of less than 1% based on finite strain theory [16–19]. In addition, the reference models of pure Ru_2P and Ru were fabricated for comparison. Fig. 5a shows the schematic models of Ru-Ru_2P [110] heterostructure, Ru_2P, and Ru with an adsorbed hydrogen atom (H^*) at their optimal sites. Fig. 5b reveals that the calculated ΔG_{H^*} value of Ru-Ru_2P is 0.034 eV, which is superior to that of pure Ru_2P (−0.178 eV) and Ru (−0.226 eV), demonstrating the highest intrinsic activity for the Ru-Ru_2P heterostructure. Notably, the optimal catalytic active site for Ru-Ru_2P is the P site at their interface, which is rationalized *via* the comparison with the ΔG_{H^*} values at other sites (Fig. S8). Considering the initial step of HER electrocatalysis in alkaline media is H_2O adsorption on a catalyst surface, the H_2O molecule adsorption energies ($\Delta E_{H_2O^*}$) on various sites of the Ru-Ru_2P [110] heterostructure were also calculated. Fig. S9 shows that the Ru site at the heterointerface possesses a lower $\Delta E_{H_2O^*}$ value of −0.239 eV than other sites, indicating the favorable H_2O adsorption site located at the heterointerface. Therefore, we tentatively propose the possible HER electrocatalysis route for Ru-Ru_2P heterostructure in alkaline media.

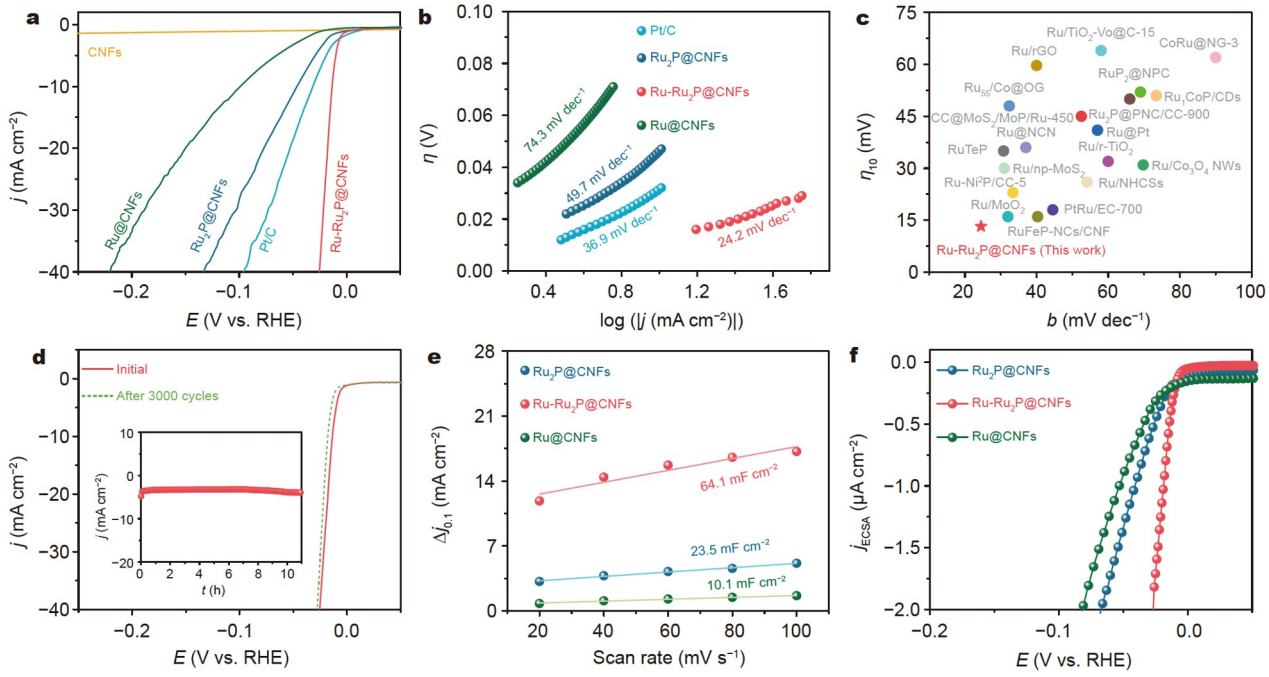

Figure 4 (a) LSV curves and (b) Tafel plots of the electrocatalysts for HER in 1 mol L^{-1} KOH. (c) Comparison of overpotential at 10 mA cm^{-2} (η_{10}) and Tafel slope (b) for Ru-Ru_2P@CNFs with the recently reported Ru-based electrocatalysts in 1 mol L^{-1} KOH. (d) LSV curves of Ru-Ru_2P@CNFs before and after 3000 CV cycles in 1 mol L^{-1} KOH. Inset: Long-term electrolysis of Ru-Ru_2P@CNFs at an overpotential of 10 mV in 1 mol L^{-1} KOH. (e) Capacitive currents as a function of scan rate and (f) ECSA-normalized LSV curves for Ru_2P@CNFs, Ru-Ru_2P@CNFs, and Ru@CNFs in 1 mol L^{-1} KOH.

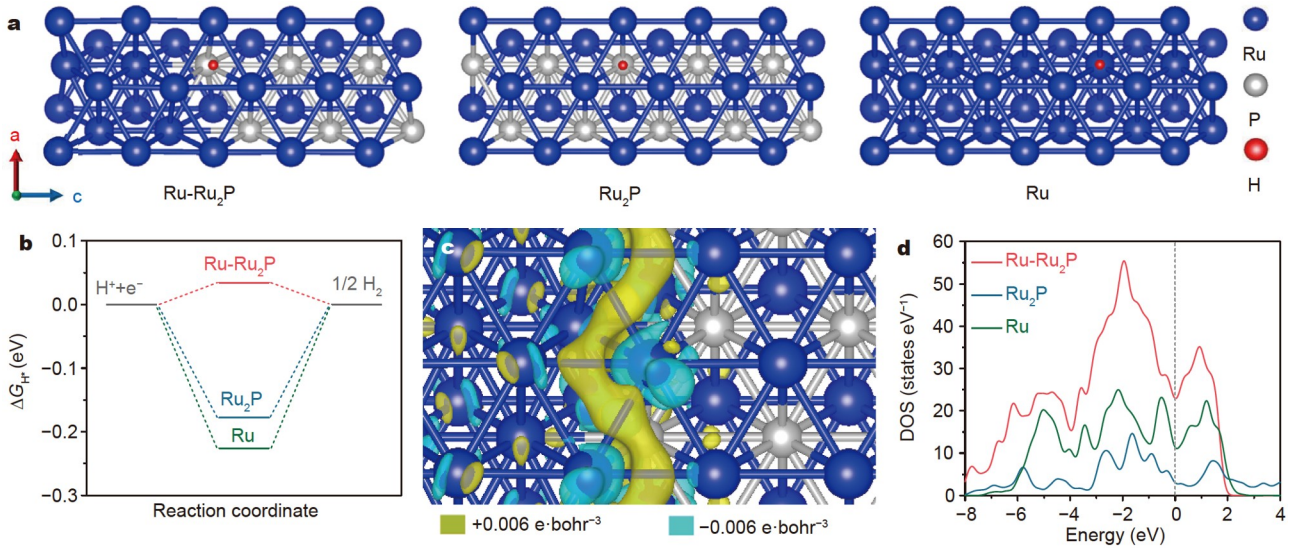

Figure 5 (a) Schematic models of Ru-Ru_2P heterostructure, Ru_2P, and Ru with H^* at their optimal catalytic active sites. (b) Calculated ΔG_{H^*} values for Ru-Ru_2P heterostructure, Ru_2P, and Ru. (c) Charge density-difference plots at the Ru-Ru_2P heterointerface. (d) The calculated electronic DOS for Ru-Ru_2P heterostructure, Ru_2P, and Ru. The Fermi level was set as 0 eV.

Fig. S10 illustrates that the H_2O molecule adsorption first occurs at the heterointerface Ru site. Afterward, the site may experience H_2O splitting with the transfer adsorption of the H atom on the adjacent P site and desorption of OH^- into the electrolyte, followed by the H_2 generation process.

The differential charge transfer analysis for the Ru-Ru_2P heterostructure was investigated. Fig. 5c shows that the interface charge redistribution along with electron transfer from Ru_2P to Ru is due to the formation of Ru-Ru_2P heterostructure, thereby effectively modulating the electronic structure at the heterointerface region. Furthermore, the density of the states (DOSs) for the Ru-Ru_2P heterostructure, pure Ru_2P, and Ru was calculated. Fig. 5d shows that the Ru-Ru_2P heterostructure possesses a higher electron density at the Fermi level than pure Ru_2P and Ru, indicating a high electrical conductivity for the Ru-Ru_2P heterostructure to achieve rapid electron transfer during the HER electrocatalysis [18]. The aforementioned DFT analysis indicates that the integration of Ru and Ru_2P to form Ru-Ru_2P heterostructures could optimize the electronic structure with enhanced catalytic active sites and increased electrical conductivity in comparison with the individual components Ru and Ru_2P, thereby achieving a significantly boosted intrinsic HER catalytic activity.

Extension to other TMP-based nanofibers

Ni, Cu, Mo, and W phosphide-based nanofibers have been identically synthesized by only altering the feeding source from $RuCl_3$ to other transition metal salts to demonstrate the versatility of the overall synthetic strategy. Fig. S11 shows the SEM images of the continuous electrospun hybrid nanofibers of Ni-PA@PAN, Cu-PA@PAN, Mo-PA@PAN, and W-PA@PAN. The resultant TMP-based nanofibers of $Ni_{12}P_5$-Ni_2P@CNFs, Cu-Cu_3P@CNFs, MoP@CNFs, and WP@CNFs have been successfully obtained after the pyrolysis, as first evidenced by the XRD patterns in Fig. 6a–d. SEM images of these samples show that the 1D nanofiber morphologies are well maintained, except for the decreased diameter of nanofibers (Fig. 6e–h). Fig. 6i–l indicate that the corresponding TEM images confirm their nanofiber morphologies decorated with numerous small nanoparticles. The HRTEM images in Fig. 6m–p reveal the effectively resolved lattice fringes consistent with the formation of $Ni_{12}P_5$-Ni_2P, Cu-Cu_3P, MoP, and WP nanoparticles embedded in carbon nanofibers for $Ni_{12}P_5$-Ni_2P@CNFs, Cu-Cu_3P@CNFs, MoP@CNFs, and WP@CNFs, respectively. In addition, the XPS and EDX characterizations in Figs S12–S14 further demonstrate the successful fabrication of $Ni_{12}P_5$-Ni_2P@CNFs, Cu-Cu_3P@CNFs, MoP@CNFs, and WP@CNFs.

CONCLUSIONS

In summary, we demonstrate the fabrication of Ru-Ru_2P@CNF catalysts *via* a synthetic strategy involving electrospinning and temperature-controlled pyrolysis treatment. The pyrolysis temperature plays a dominant role in the morphology and composition of resultant catalysts. The catalysts experience a composition conversion from pure Ru_2P to heterostructured Ru-Ru_2P and pure Ru with an increase in pyrolysis temperature. The optimized catalyst Ru-Ru_2P@CNFs comprise heterostructured Ru-Ru_2P nanoparticles that are embedded in N,P-codoped CNFs. This result indicates the outstanding HER catalytic performances in acidic and alkaline media, which are superior to those of Ru_2P@CNFs, Ru@CNFs, 20% Pt/C, and the recently reported Ru-based electrocatalysts. DFT calculations reveal that the electronic coupling interactions between Ru and Ru_2P components could achieve a well-modulated electronic structure at the heterointerface, which results in optimized catalytic active sites and promotes electrical conductivity for enhanced HER electrocatalysis. Moreover, the overall synthetic strategy has been extended to fabricate TMP-based nanofibers, which may find broad applications in the fields of catalysis and energy storage and conversion. This study not only demonstrates a deep insight into the electronic structure modulation by interfacial engineering but also provides a facile strategy to develop 1D

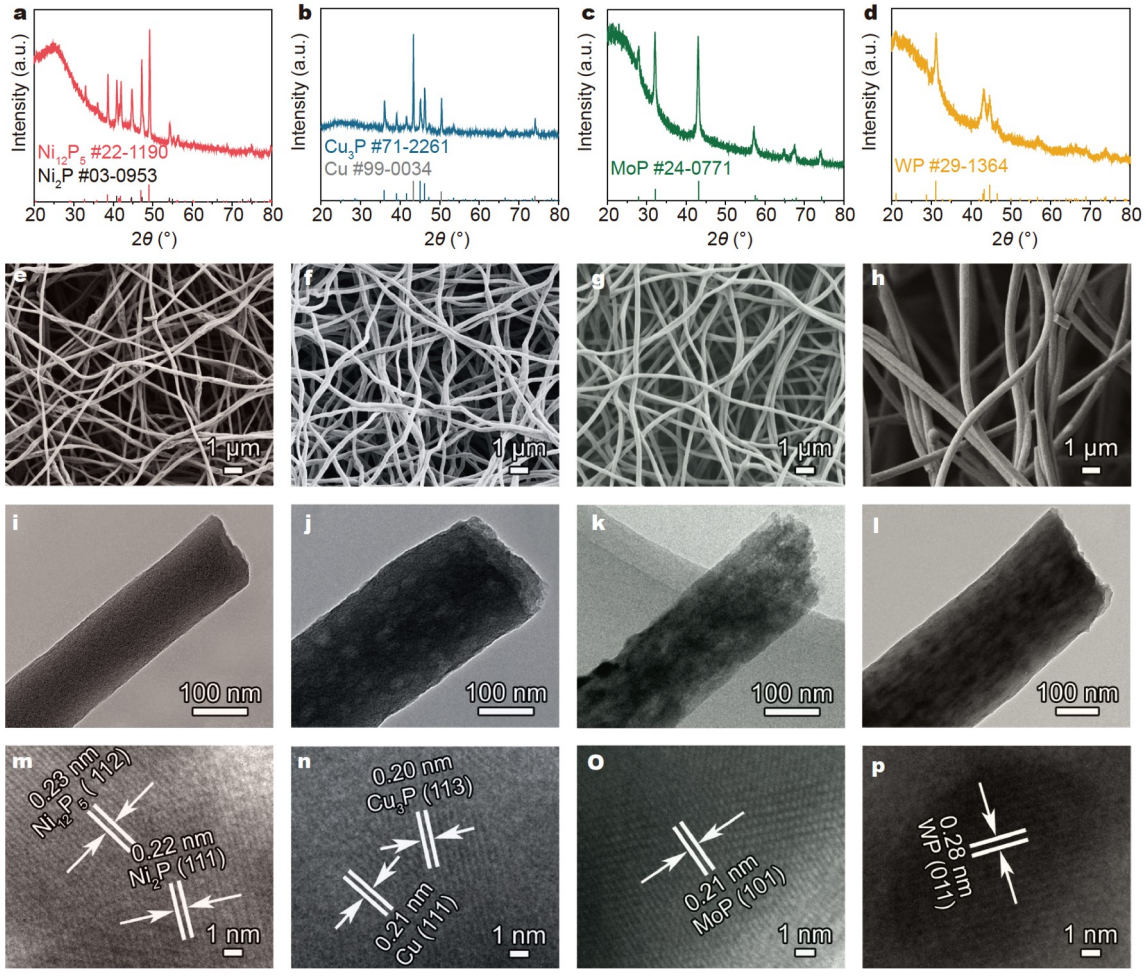

Figure 6 (a–d) XRD patterns, (e–h) SEM images, (i–l) TEM images, and (m–p) HRTEM images of (a, e, i, m) $Ni_{12}P_5$-Ni_2P@CNFs, (b, f, j, n) Cu-Cu_3P@CNFs, (c, g, k, o) MoP@CNFs, and (d, h, l, p) WP@CNFs, respectively.

nanostructured catalysts with high conductivity and activity for electrocatalysis and beyond.

Received 2 January 2022; accepted 17 February 2022; published online 28 April 2022

1 Sun L, Luo Q, Dai Z, *et al.* Material libraries for electrocatalytic overall water splitting. Coord Chem Rev, 2021, 444: 214049
2 Yu ZY, Duan Y, Feng XY, *et al.* Clean and affordable hydrogen fuel from alkaline water splitting: Past, recent progress, and future prospects. Adv Mater, 2021, 33: 2007100
3 Wang YZ, Yang M, Ding YM, *et al.* Recent advances in complex hollow electrocatalysts for water splitting. Adv Funct Mater, 2022, 32: 2108681
4 Wang M, Zhang L, He Y, *et al.* Recent advances in transition-metal-sulfide-based bifunctional electrocatalysts for overall water splitting. J Mater Chem A, 2021, 9: 5320–5363
5 Zhang B, Zheng Y, Ma T, *et al.* Designing MOF nanoarchitectures for electrochemical water splitting. Adv Mater, 2021, 33: 2006042
6 Li Y, Sun Y, Qin Y, *et al.* Recent advances on water-splitting electrocatalysis mediated by noble-metal-based nanostructured materials. Adv Energy Mater, 2020, 10: 1903120
7 Zhu J, Hu L, Zhao P, *et al.* Recent advances in electrocatalytic hydrogen evolution using nanoparticles. Chem Rev, 2020, 120: 851–918
8 Yang Y, Yu Y, Li J, *et al.* Engineering ruthenium-based electrocatalysts for effective hydrogen evolution reaction. Nano-Micro Lett, 2021, 13: 160
9 Bae SY, Mahmood J, Jeon IY, *et al.* Recent advances in ruthenium-based electrocatalysts for the hydrogen evolution reaction. Nanoscale Horiz, 2020, 5: 43–56
10 Zheng Y, Jiao Y, Zhu Y, *et al.* High electrocatalytic hydrogen evolution activity of an anomalous ruthenium catalyst. J Am Chem Soc, 2016, 138: 16174–16181
11 Liu T, Wang S, Zhang Q, *et al.* Ultrasmall Ru_2P nanoparticles on graphene: A highly efficient hydrogen evolution reaction electrocatalyst in both acidic and alkaline media. Chem Commun, 2018, 54: 3343–3346
12 Ji L, Lv C, Chen Z, *et al.* Nickel-based (photo)electrocatalysts for hydrogen production. Adv Mater, 2018, 30: 1705653
13 Li Z, Hu M, Wang P, *et al.* Heterojunction catalyst in electrocatalytic water splitting. Coord Chem Rev, 2021, 439: 213953
14 Xu Q, Zhang J, Zhang H, *et al.* Atomic heterointerface engineering overcomes the activity limitation of electrocatalysts and promises highly-efficient alkaline water splitting. Energy Environ Sci, 2021, 14: 5228–5259
15 Zhang H, Maijenburg AW, Li X, *et al.* Bifunctional heterostructured transition metal phosphides for efficient electrochemical water splitting. Adv Funct Mater, 2020, 30: 2003261
16 Liu T, Li A, Wang C, *et al.* Interfacial electron transfer of Ni_2P-NiP_2 polymorphs inducing enhanced electrochemical properties. Adv Mater, 2018, 30: 1803590
17 Liu C, Gong T, Zhang J, *et al.* Engineering Ni_2P-$NiSe_2$ heterostructure interface for highly efficient alkaline hydrogen evolution. Appl Catal B-Environ, 2020, 262: 118245

18 Zeng L, Sun K, Wang X, *et al.* Three-dimensional-networked Ni_2P/Ni_3S_2 heteronanoflake arrays for highly enhanced electrochemical overall-water-splitting activity. Nano Energy, 2018, 51: 26–36
19 Ji L, Wei Y, Wu P, *et al.* Heterointerface engineering of Ni_2P-Co_2P nanoframes for efficient water splitting. Chem Mater, 2021, 33: 9165–9173
20 Wang G, Chen W, Chen G, *et al.* Trimetallic Mo-Ni-Co selenides nanorod electrocatalysts for highly-efficient and ultra-stable hydrogen evolution. Nano Energy, 2020, 71: 104637
21 Huang J, Wen S, Chen G, *et al.* Multiphase Ni-Fe-selenide nanosheets for highly-efficient and ultra-stable water electrolysis. Appl Catal B-Environ, 2020, 277: 119220
22 Li SH, Qi MY, Tang ZR, *et al.* Nanostructured metal phosphides: From controllable synthesis to sustainable catalysis. Chem Soc Rev, 2021, 50: 7539–7586
23 Zhang Z, Wu X, Kou Z, *et al.* Rational design of electrospun nanofiber-typed electrocatalysts for water splitting: A review. Chem Eng J, 2022, 428: 131133
24 Wang J, Li X, Zhang T, *et al.* Electro-reforming polyethylene terephthalate plastic to Co-produce valued chemicals and green hydrogen. J Phys Chem Lett, 2022, 13: 622–627
25 Lu X, Li M, Wang H, *et al.* Advanced electrospun nanomaterials for highly efficient electrocatalysis. Inorg Chem Front, 2019, 6: 3012–3040
26 Zhang CL, Yu SH. Nanoparticles meet electrospinning: Recent advances and future prospects. Chem Soc Rev, 2014, 43: 4423–4448
27 Noerskov JK, Bligaard T, Logadottir A, *et al.* Trends in the exchange current for hydrogen evolution.. ChemInform, 2005, 36
28 Chi XY, Xia BG, Xu ZL, *et al.* Impact of cross-linked chitosan sublayer structure on the performance of TFC FO PAN nanofiber membranes. ACS Omega, 2018, 3: 13009–13019
29 Zhang M, Chen R, Liu X, *et al.* Anticorrosion study of phytic acid ligand binding with exceptional self-sealing functionality. J Alloys Compd, 2020, 818: 152875
30 Chen YY, Zhang Y, Jiang WJ, *et al.* Pomegranate-like N,P-doped Mo_2C@C nanospheres as highly active electrocatalysts for alkaline hydrogen evolution. ACS Nano, 2016, 10: 8851–8860
31 Zhao R, Liu C, Zhang X, *et al.* An ultrasmall Ru_2P nanoparticles-reduced graphene oxide hybrid: An efficient electrocatalyst for NH_3 synthesis under ambient conditions. J Mater Chem A, 2020, 8: 77–81
32 Ji L, Zheng H, Wei Y, *et al.* Temperature-controlled fabrication of Co-Fe-based nanoframes for efficient oxygen evolution. Sci China Mater, 2022, 65: 431–441
33 Song W, Teng X, Liu Y, *et al.* Rational construction of self-supported triangle-like MOF-derived hollow (Ni,Co)Se_2 arrays for electrocatalysis and supercapacitors. Nanoscale, 2019, 11: 6401–6409

Acknowledgements This work was financially supported by the Natural Science Foundation of Zhejiang Province (LQ20B030001 and LY20E020002) and China Postdoctoral Science Foundation (2021M702305).

Author contributions Wei Y conducted the experiment and wrote the paper. Xu G conducted the DFT calculations and analyzed the data; Wei Y and Wang T did some characterizations; Ji L, Liu Z, and Wang S supervised this study and revised the paper. All authors contributed to the general discussion.

Conflict of interest The authors declare that they have no conflict of interest.

Supplementary information Supporting data are available in the online version of the paper.

Yue Wei received her BSc degree from Hubei Engineering University in 2019. She is currently an MSc degree student under the supervision of Prof. Sheng Wang and Dr. Lvlv Ji at Zhejiang Sci-Tech University. Her research interests focus on the nanofibrous materials for electrocatalytic hydrogen production.

Lvlv Ji is currently a lecturer at Zhejiang Sci-Tech University. He received his BSc degree from Huainan Normal University in 2012, MSc degree from Zhejiang University of Technology in 2015, and PhD degree from Tongji University in 2018. His research interests focus on electrocatalysis, and energy storage and conversion.

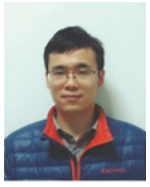

Zhun Liu received his PhD degree from Beijing University of Technology in 2017. He worked as an assistant researcher at Jilin University from 2017 to 2019, and then worked at the South China Normal University from 2019 to 2021. He joined the Department of Physics, Shaoxing University in 2021. His research interests focus on electronic materials and their devices for energy conversion, information functional materials, and computational materials science.

Sheng Wang received his PhD degree from Fukui University, Japan in 2003, and then worked as assistant lecturer at Hokkaido University for three years. He joined Zhejiang Sci-Tech University in 2006 and was promoted to a full professor in 2013. His research interests include nano photocatalysis, bio-inspired strategies for functional nanomaterials, and micro/nano fibrous composites.

温度调控合成异质结构Ru-Ru_2P纳米颗粒负载碳纳米纤维用于高效电催化析氢反应

韦悦[1], 徐杲[2], 韦渝洁[1], 纪律律[1*], 王驹[1], 刘准[2*], 王晟[1*]

摘要 开发高效、低价、稳定的析氢催化剂是实现电解水制氢规模产业化的关键, 但仍面临巨大挑战. 在本文中, 我们通过静电纺丝和控温热处理的合成路径制备了一种高活性Ru基催化剂材料, 该催化剂由异质结构Ru-Ru_2P纳米颗粒均匀负载于N、P共掺杂碳纳米纤维构成. 所制备的Ru-Ru_2P异质催化剂表现出优异的电催化析氢活性, 在酸性和碱性电解液中产生10 mA cm^{-2}的催化电流密度分别仅需11和14 mV的过电位, 其性能优于对比样品纯Ru和纯Ru_2P催化剂. 密度泛函理论计算结果表明在Ru和Ru_2P的异质界面处存在电子耦合效应, 从而有效调控催化剂界面电子结构, 优化活性位点氢吸附能并提高导电性, 实现了高效电催化析氢. 本合成策略适用于制备一系列过渡金属磷化物纳米纤维, 因而在催化和储能等领域具有广泛的应用前景.

